View Article Online
View Journal

Nanoscale Horizons

The home for rapid reports of exceptional significance in nanoscience and nanotechnology

Accepted Manuscript

This article can be cited before page numbers have been issued, to do this please use: A. Shah, S. Jain, Y. Zhang, G. Liu and V. K. Sharma, *Nanoscale Horiz.*, 2026, DOI: 10.1039/D6NH00181E.

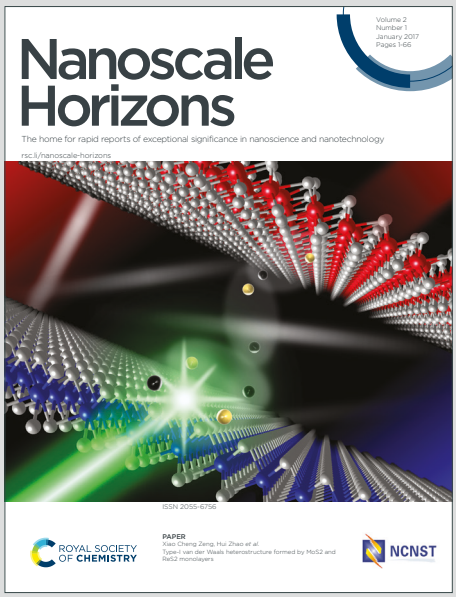

View Article Online
DOI: 10.1039/D6NH00181E

New Concept Statement

This work establishes a new materials design concept that bridges block copolymer-directed nanostructuring with bimetallic functionality to engineer multifunctional adsorption platforms. Rather than treating pore architecture and surface chemistry as independent variables, we demonstrate that RAFT-derived block copolymers can act as integrated structure-directing and chemical templating agents, enabling simultaneous control over hierarchical porosity and spatial distribution of metal species during carbonization.

The key conceptual advance lies in leveraging nanoscale phase separation to direct the formation of uniformly dispersed copper and nickel oxides heterointerfaces within a conductive carbon framework. This approach generates a chemically heterogeneous yet structurally continuous network of adsorption sites, where electrostatic interactions, π–π coupling, and metal-centered coordination can be synergistically tuned. As a result, the material exhibits dual-function adsorption capability toward both anionic and cationic dyes, overcoming the inherent selectivity limitations of conventional adsorbents.

More broadly, this work introduces a generalizable strategy for coupling polymer chemistry with multimetallic nanostructuring to design adaptive and multifunctional carbon materials. This concept opens new directions for the rational development of next-generation adsorbents and extends to applications in catalysis, separations, and energy-related systems.

View Article Online
DOI: 10.1039/D6NH00181E

Bimetallic Cu/Ni-Doped Porous Carbon Fibers as High-Performance Adsorbents for Organic Dyes

Akshara Paras Parekh[a,b], Shilpa Jain[c], Vinay Sharma[d], Yue Zhang[a], Guoliang Liu[a,e,f*]

[a]Department of Chemistry, Virginia Tech, Blacksburg, VA 24061, USA

[b]Department of Engineering Sciences and Humanities, Thakur College of Engineering and Technology, Mumbai, Maharashtra, India

[c]Department of Chemistry, Jai Hind College, Mumbai - 400020, India

[d]Research and Development Cell (RDC), Parul Institute of Applied Sciences (PIAS), Parul University, Vadodara, Gujarat 391760, India

[e]Macromolecules Innovation Institute, Virginia Tech, Blacksburg, VA 24061, USA

[f]Division of Nanoscience, Academy of Integrated Science, Virginia Tech, Blacksburg, VA 24061, USA

Abstract:

The increasing amount of synthetic dye pollutants in industrial wastewater poses significant environmental and health concerns, creating an urgent need for efficient and sustainable remediation strategies. Herein, we report the fabrication of bimetallic Cu-Ni oxide doped porous carbon nanofibers (Cu:Ni:PCF) via block copolymer templating, electrospinning, and controlled pyrolysis. The hierarchical structures combined with uniformly dispersed copper and nickel oxide nanoparticles within the carbon matrix, provided abundant active sites, enhanced surface charge modulation, and multifunctional adsorption capabilities. The Cu:Ni:PCF adsorbent demonstrated excellent uptake of anionic MO and cationic MB, reaching Langmuir maximum monolayer adsorption capacities of 362 mg g^{-1} for MO and 323 mg g^{-1} for MB, showing enhanced localized single-point capacities under optimized pH environments. Rapid adsorption kinetics were observed, reaching equilibrium within 15 min. The kinetics data were best described by a pseudo-second-order model, indicating a strong adsorption interaction. The equilibrium data fit the Langmuir isotherm model, suggesting monolayer coverage on uniform adsorption sites. Notably, the adsorbent maintained its structural integrity and demonstrated high recyclability, retaining more than 90% of its initial adsorption capacity

View Article Online
DOI: 10.1039/D6NH00181E

after five consecutive adsorption–desorption cycles. These findings underscore the potential of Cu:Ni:PCF as a durable and efficient material for removing various dye contaminants from wastewater, representing a promising strategy for practical environmental remediation.

Keywords: Porous Carbon Nanofibers, Electrospun Nanofibers, Bimetallic nanocomposite, Dye Adsorption, Wastewater Treatment.

View Article Online
DOI: 10.1039/D6NH00181E

1. Introduction

The continuous expansion of industrial activities and urban development has markedly increased the volume and complexity of wastewater discharged into natural water bodies. Such uncontrolled release of contaminated effluents can severely disrupt aquatic ecosystems, leading to ecological imbalances, accumulation of toxic substances, and impaired photosynthetic function in aquatic plants, ultimately threatening overall biodiversity.[1,2] Among the various pollutants present in industrial effluents, synthetic dyes are particularly problematic due to their extensive use in textile, plastic, paper, pharmaceutical, and cosmetic products. The intrinsic chemical stability of these dyes renders them resistant to conventional biological degradation.[3,4] Industrial dyes such as methylene blue (MB) and methyl orange (MO) are known to pose significant risks to human health, including effects on breathing and brain function, organ toxicity, cardiovascular dysfunction, and dermatological complications. These dyes possibly inhibit photosynthetic processes in aquatic and terrestrial flora.[5-8]

These environment- and health-related challenges demand the development of efficient strategies for removing dye contaminants from wastewater, which has become an urgent global priority.[9] Numerous technologies have been explored for dye remediation, including adsorption,[10-12] advanced oxidation processes,[13] electrochemical treatment,[14] and photocatalytic degradation.[15-17] Although these methods offer promising performance, they are often limited by high operational costs, slow reaction rates, high energy demands, and sometimes, the generation of secondary pollutants. By comparison, adsorption stands out as a highly effective and versatile treatment due to its rapid sorption kinetics, high removal efficiency, ease of operation, cost-effectiveness, and broad range of available adsorbent materials.[18-19] Through designing tailored adsorbents, adsorption-based processes provide a robust and sustainable pathway for removing organic dye contaminants in aquatic systems.

For effective adsorption of organic dyes, semiconductor-based materials must exhibit efficient charge separation, rapid carrier transport, and appropriate bandgaps.[20] Cuprous and copper oxides with narrow band gap (~1.35 eV) along with p-type conductivity and natural abundance, have emerged as appealing candidates among semiconducting metal oxides.[21, 22] They introduce redox-active and Lewis acidic sites into the porous carbon framework, enabling enhanced electrostatic interactions, and charge tunability towards both anionic and cationic dyes. However, the limited oxidation resistance often diminishes its long-term stability and performance. Coupling them with a secondary metal oxide such as NiO offers an avenue to

View Article Online
DOI: 10.1039/D6NH00181E

overcome these drawbacks. The formation of bimetallic-oxide heterojunctions can enhance charge transfer, suppress recombination, and improve overall structural durability. Despite these advantages, metal oxides encounter challenges in practical applications, including particle agglomeration and limited recyclability. These limitations can be alleviated by dispersing metal oxides on conductive, high surface area supports such as carbon fibers and nanotubes, which help maintain particle dispersion while providing additional adsorption sites.[23,24]

The porous architecture of an adsorbent plays a critical role in determining mass transport and adsorption capacity. Traditional approaches (e.g., chemical activation or exfoliation) for fabricating porous carbon nanofibers frequently led to poorly controlled pore distributions and compromised mechanical integrity.[25,26] An alternative and more tunable route is to use block copolymer templates, which undergo microphase separation to create well-ordered nanoscale morphologies.[27,28,29] Upon pyrolysis, polyacrylonitrile (PAN)-based block copolymers generate porous carbon fibers (PCF) with hierarchical micro-, meso-, and macro-porous networks. This multiscale architecture offers enhanced surface area, structural robustness, and rapid fluid infiltration.[30,31] Incorporating bimetallic oxides into these PCF enables modulation of pore size and surface chemistry, resulting in materials with superior adsorption efficacy toward a variety of dye molecules.[32]

We report a strategy for the synthesis of porous carbon fiber doped with Cu_2O/CuO (Cu:PCF), NiO (Ni:PCF), and copper and nickel oxides (Cu:Ni:PCF) via a controlled block copolymer templating approach. By integrating bimetallic oxide functionalities within a hierarchically porous carbon framework, the resulting materials are designed to provide multifunctional adsorption interfaces for the removal of both anionic and cationic dyes. The resulting nanocomposites feature a well-defined mesoporous architecture, interconnected carbon networks, and a high accessible surface area, collectively enabling rapid and efficient adsorption of dye molecules. They are systematically investigated for adsorption performance, kinetics, and thermodynamic behaviour for efficient removal of MO and MB in aqueous systems. Overall, this work demonstrates a versatile strategy for designing high-performance, regenerable adsorbents for removing dye contaminants from aqueous systems.

View Article Online
DOI: 10.1039/D6NH00181E

2. Experimental Section

2.1 Materials

All reagents were of analytical grade and used as received unless otherwise specified. Acrylonitrile (AN, ≥99%), methyl methacrylate (MMA, ≥99%), benzene (≥99.9%), activated neutral alumina (Brockmann Activity I), cumyl dithiobenzoate (CDB, ≥99%), 2,2′-azobis(2-methylpropionitrile) (AIBN, ≥98%), and N,N-dimethylformamide (DMF, ≥99.7%) were sourced from Sigma-Aldrich. Copper acetate, nickel acetate, methyl orange (MO), methylene blue (MB), potassium hydroxide (KOH), sodium hydroxide (NaOH), and hydrochloric acid (HCl) were also obtained from the same supplier. Before polymerization, inhibitor species were removed from AN and MMA by passing them through activated alumina columns, whereas the remaining reagents were used as received.

2.2 Synthesis of PAN-b-PMMA block copolymer

The PAN-b-PMMA block copolymer was prepared using a reversible addition–fragmentation chain-transfer (RAFT) polymerization approach. In the first step, MMA, CDB, and AIBN were dissolved in benzene within a Schlenk flask. The reaction mixture was subjected to three freeze-pump-thaw cycles to remove dissolved gases, followed by nitrogen back-filling. Polymerization was then conducted at 60 °C for 24 h under continuous stirring to generate the PMMA macro-chain transfer agent (macro-CTA). The resulting polymer was isolated by precipitation in methanol and subsequently dried under reduced pressure. In the second step, the obtained PMMA macro-CTA was chain-extended with AN in the presence of AIBN using dimethyl sulfoxide (DMSO) as the reaction medium. After degassing, the reaction system was maintained at 65 °C for 24 h under an inert atmosphere. The final PAN-b-PMMA block copolymer was recovered using the same purification procedure.

2.3 Synthesis of CuNi-doped porous carbon fibers

For porous carbon fiber fabrication, PAN-b-PMMA (0.8 g) was dissolved in DMF to form a uniform polymer solution. Copper and nickel acetate salts were incorporated, and the mixture was stirred for several hours to ensure homogeneous distribution of the metal precursors. The resulting solution was transferred into a syringe and processed via electrospinning using optimized parameters (tip-to-collector distance: 20 cm; flow rate: 0.35 mL h^{-1}; applied voltage: 20 kV. The collected fibers were subjected to stabilization, followed by carbonization under a controlled thermal program to obtain Cu:Ni:PCF (Figure 1). It should be noted that the obtained

View Article Online
DOI: 10.1039/D6NH00181E

nanofibrous Cu:Ni:PCF was subsequently ground into powder for the wastewater treatment. For comparison, copper oxide, nickel oxides and PCF were synthesized by electrospinning.

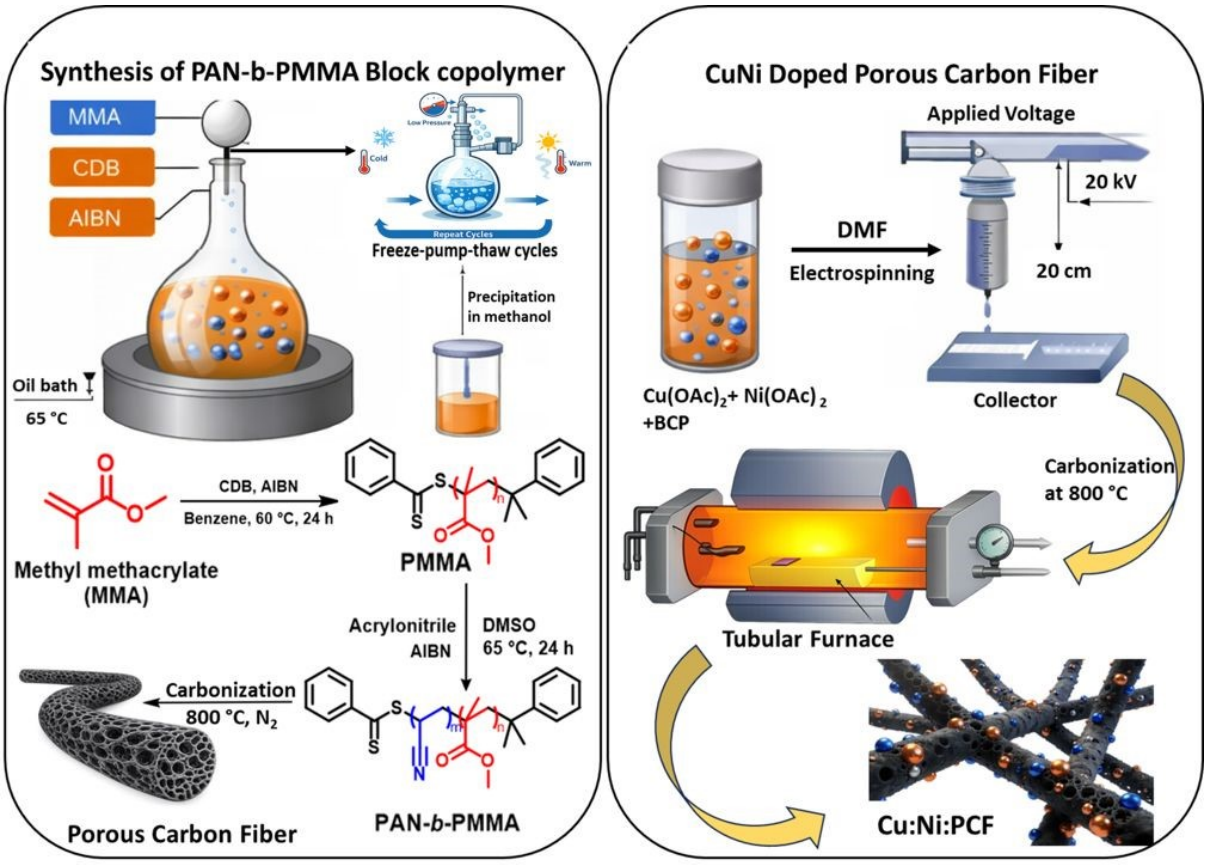

Figure 1: Schematic illustration of (left) the synthesis of PAN-*b*-PMMA via RAFT polymerization and (right) the processing of PAN-*b*-PMMA with Cu and Ni salts into Cu:Ni:PCF fibers via electrospinning and pyrolysis.

2.4 Material characterization

Phase composition was examined using X-ray diffraction (XRD) on a Rigaku Miniflex 600 instrument. The morphology and microstructural features were examined by field-emission scanning electron microscopy (FE-SEM, Hitachi SU8010, Japan) and high-resolution transmission electron microscopy (HR-TEM, JEOL JEM-F200). Porous characteristics were determined from nitrogen adsorption–desorption measurements at 77 K, and the specific surface area was derived using the Brunauer–Emmett–Teller (BET) model.

Surface chemical composition and oxidation states were probed using X-ray photoelectron spectroscopy (XPS, PHI 5000 VersaProbe II) by employing Al Kα radiation (hν = 1486.6 eV),

View Article Online
DOI: 10.1039/D5NH00181E

with binding energy calibration referenced to the C 1s peak at 284.7 eV. The surface charge behavior was evaluated via ζ-potential measurements using a Zetasizer Nano ZS90. Optical absorption properties were recorded using a UV–visible spectrophotometer (TU-1810).

2.5 Adsorption of dyes

A stock solution (200 mg L^{-1}) of each dye was prepared and subsequently diluted to obtain working concentrations of MO and MB. The influence of various parameters, including initial dye concentration, adsorbent dosage, contact duration, pH, and temperature, was systematically assessed. In a typical adsorption test, a fixed amount of Cu:Ni:PCF was introduced into 50 mL of dye solution and stirred at 400 rpm at 25 °C. Samples were withdrawn at defined time intervals, and the residual dye concentration was quantified using UV–visible spectroscopy. The equilibrium adsorption capacity (q_e, %) were R using equations 1 and 2.[33-35]

$$q_e = \frac{(c_0 - c_e)V}{m} \quad (1)$$

$$r(\%) = \frac{(c_0 - c_e)}{c_0} x\ 100\% \quad (2)$$

where C_0 and C_e (mg L^{-1}) represent the initial and equilibrium dye concentrations, respectively, V(mL) is the solution volume, and m(g) is the mass of the adsorbent.

Thermodynamic parameters were determined to assess the nature of the adsorption process. The standard enthalpy change (ΔH°) and entropy change (ΔS°) were obtained from the Van't Hoff relationship (eq 3),

$$\ln K^\circ = \frac{\Delta S^o}{R} - \frac{\Delta H^o}{RT} \quad (3)$$

where R(8.314 J mol^{-1} K^{-1}) is the universal gas constant and T(K) is the absolute temperature. The thermodynamic equilibrium constant K° was estimated using eq 4:

$$K^\circ = \frac{q_e}{C_e} \quad (4)$$

The values of ΔH° and ΔS° were determined from the slope and intercept of the linear Van't Hoff plot ($\ln K^\circ$ versus $1/T$), respectively.

View Article Online
DOI: 10.1039/D6NH00181E

3. Results and Discussion

Synthesis and characterization of Cu- and Ni-doped PCF.

A PAN-b-PMMA block copolymer was prepared through a reversible addition–fragmentation chain-transfer (RAFT) polymerization route and subsequently utilized as the carbon precursor for nanofiber fabrication. The molecular characteristics of the intermediate PMMA segment and the resulting diblock copolymer were evaluated using proton nuclear magnetic resonance (^{1}H NMR) spectroscopy in combination with size exclusion chromatography (SEC). The PMMA macro-chain exhibited a number-average molecular weight (M□) of approximately 46 kDa with a narrow dispersity (Đ = 1.08), while successful chain extension yielded the PAN-b-PMMA copolymer with an increased M□ of ~158 kDa and a dispersity of 1.13 (Figure S1). The block copolymer was processed into porous carbon fibers, with and without nanoparticles, via electrospinning and pyrolysis. The final morphologies of the fibrous materials were characterized using FE-SEM with Energy Dispersive Spectroscopy (EDS) and HR-TEM (Figure 2). Cu:Ni:PCF nanofibers showed well-controlled fiber diameters and smooth surfaces, as well as interconnected pores (Figure 2a-b). High-resolution FE-SEM images revealed copper and nickel oxide nanoparticles uniformly embedded within the porous carbon fibers, and some on the outer fiber surface. These nanoparticles contributed to structural heterogeneity and readily accessible adsorption sites for dye removal. HR-TEM images of Cu:Ni:PCF showed densely packed particles (Figure 2c-e). The interconnected internal and surface porosity provided an extensive surface area with a large number of exposed adsorption sites. The encapsulation of copper and nickel oxide nanoparticles within graphitic carbon, on the one hand, protected the particles from corrosion under harsh conditions, and on the other hand, enhanced the adsorption performance of the carbon matrix. The selected area electron diffraction (SAED) patterns showed diffraction features forming well-defined polycrystalline rings, suggesting enhanced particle alignment in the PCF. EDS elemental mapping (Figure 2g) confirmed homogeneous distribution of C, N, O, Cu, and Ni along the fiber, verifying successful co-immobilization of copper and nickel oxides on the PCF surface. The EDS spectrum correlated well with the EDS elemental mapping, demonstrating the homogeneous elemental dispersion within the Cu:Ni:PCF (Figure 2h).

View Article Online
DOI: 10.1039/D6NH00181E

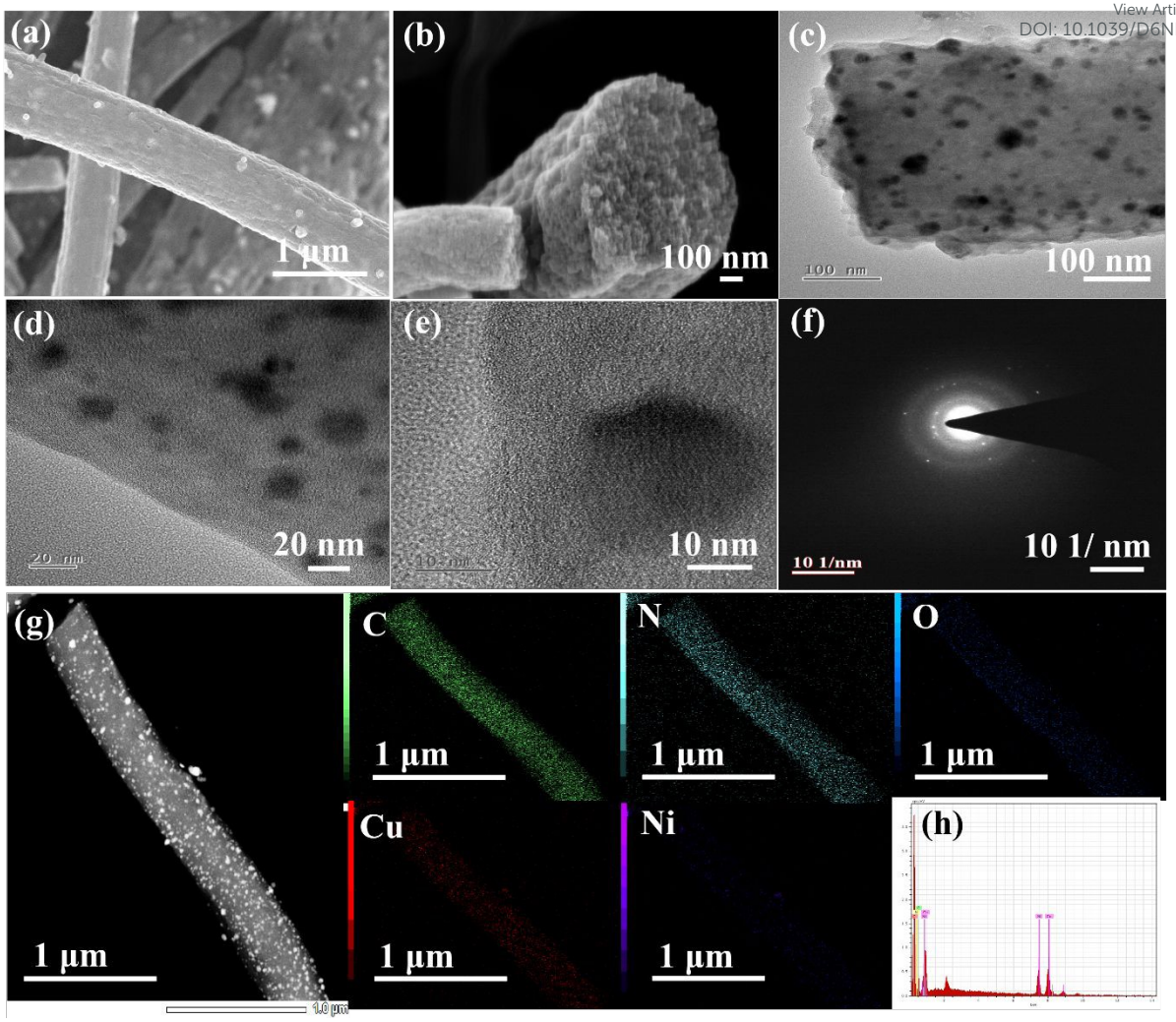

Figure 2 FE-SEM images of (a-b) Cu:Ni:PCF, (c-e) HR-TEM images of Cu:Ni:PCF, (f) SAED pattern of Cu:Ni:PCF, (g) HAADF-STEM image accompanied by EDS elemental maps demonstrating uniform elemental distribution (C, N, O, Cu, and Ni), and (h) EDAX spectra of Cu:Ni:PCF.

The diffraction pattern of PCF was characterized by an intense reflection at $2\theta \approx 24.7°$ and a minor peak near 44°, assigned to the (002) and (100) graphitic carbon planes (Figure 3a(i)).[36] The broad nature of these peaks indicates partial graphitization and disordered carbon domains, which are favorable for adsorption due to enhanced surface defects and active sites. Upon incorporation of copper oxide, the sample displayed distinct peaks at $2\theta \approx 36.7°$, 42.6°, 61.7°, and 73.9° (Figure 3a(ii)), which can be indexed to the (111), (200), (220), and (311) planes of cubic Cu_2O (JCPDS No. 05-0667).[37] In addition to these reflections, weak peaks corresponding to monoclinic CuO were observed at 38.2°, suggesting the co-existence of Cu(I) and Cu(II) oxide phases. Such mixed copper oxide formation is consistent with previous reports, where partial oxidation of Cu_2O to CuO occurred during thermal treatment, resulting in a Cu_2O/CuO

View Article Online
DOI: 10.1039/D6NH00181E

heterostructure without disrupting the overall crystal framework.[38] Ni:PCF exhibited characteristic diffraction peaks at 2θ ≈ 37.3°, 43.2°, and 63.1° (Figure 3a(iii)), corresponding to the (111), (200), and (220) planes of face centred cubic NiO (JCPDS No. 78-0429)[39], confirming the formation of crystalline nickel oxide nanoparticles uniformly embedded in the carbon matrix. For the bimetallic Cu:Ni:PCF composite, diffraction peaks associated with Cu_2O, CuO, and NiO were all present (Figure 3a(iv)), demonstrating the successful incorporation of both copper and nickel oxides into the porous carbon fibers. The absence of additional impurity peaks indicates high phase purity and effective dispersion of metal oxide nanocrystals. Notably, the relatively lower intensity and peak broadening of metal oxide reflections suggest nanoscale crystallite size and strong interaction with the carbon framework, which is advantageous for adsorption applications. The coexistence of Cu_2O/CuO and NiO phases would generate abundant heterointerfaces, facilitating enhanced surface reactivity and dye–adsorbent interactions.

Porosity and surface area were analyzed by nitrogen adsorption–desorption isotherms (Figure 3b). The BET model was applied to calculate surface area, and nonlocal density functional theory (NLDFT) was utilized to determine pore-size distribution.[40] All fibers, including PCF, Cu_2O/CuO-PCF, NiO-PCF, and the bimetallic Cu:Ni:PCF, showed type IV isotherm behavior accompanied by distinct hysteresis loops, confirming the presence of mesoporosity. The pure PCF displayed a BET surface area of 576.52 m^2g^{-1}, which decreased upon incorporation of metal oxide nanoparticles to 418.64 $m^2\ g^{-1}$ for Cu_2O-PCF, 352.97 m^2g^{-1} for NiO-PCF, and 251.42 m^2g^{-1} for the Cu:Ni:PCF composite. This reduction in surface area is attributed to partial pore occupation and structural blocking caused by the embedded oxide phases. NLDFT analysis revealed that the majority of pores fall within the mesoporous regime of 2–50 nm (Figure S2), aligning with the hysteresis features present in the adsorption isotherms. The hierarchical mesoporous network of Cu:Ni:PCF could provide abundant accessible adsorption sites and facilitate fast diffusion of dye molecules through interconnected pore channels. We anticipate such structural features to be advantageous for enhancing dye uptake efficiency and overall adsorption performance.

View Article Online
DOI: 10.1039/D6NH00181E

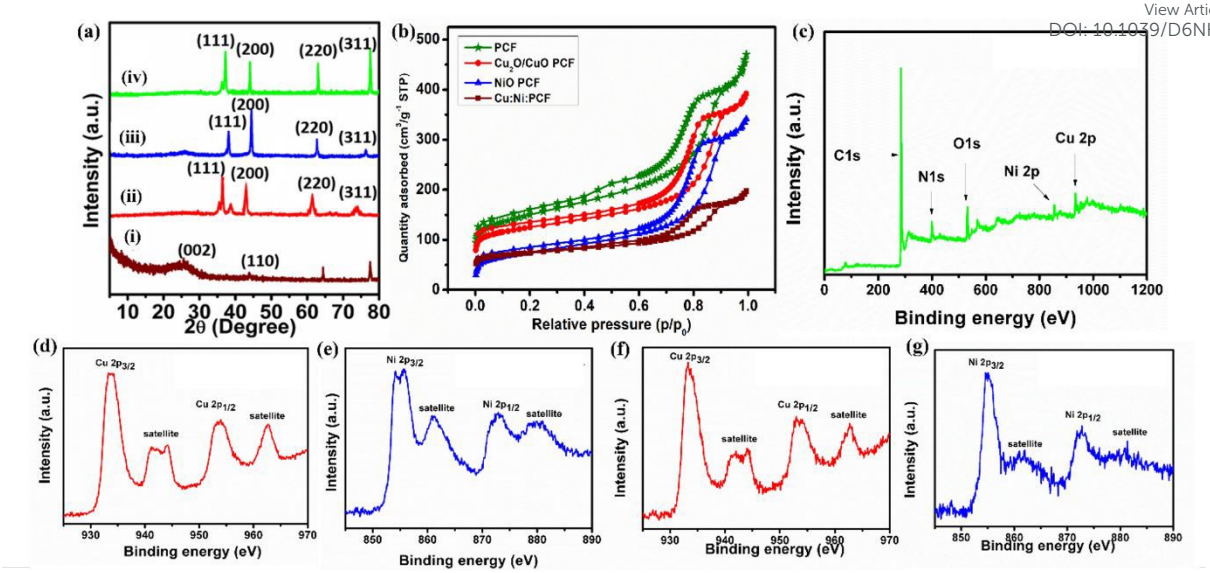

Figure 3 (a) XRD patterns of (i) PCF, (ii) Cu_2O/CuO-PCF, (iii) NiO-PCF and (iv) Cu:Ni:PCF, (b) BET profiles of PCF, Cu_2O/CuO-PCF, NiO-PCF and Cu:Ni:PCF, (c) XPS Survey spectra of Cu:Ni:CNF, XPS pattern of Cu 2p (d) Cu_2O/CuO-PCF and (f) Cu:Ni:PCF, XPS pattern of Ni 2p (e) NiO-PCF and (g) Cu:Ni:PCF.

The chemical states and surface elemental distribution of the Cu:Ni:PCF composite were characterized by X-ray photoelectron spectroscopy (XPS) (Figure 3(c-g)). XPS survey spectra (Figure S3) displayed dominant C 1s peaks with minor N 1s and O 1s peaks for PCF, confirming its carbonaceous framework. In comparison, Cu_2O/CuO:PCF and Ni:PCF exhibited characteristic Cu 2p and Ni 2p signals, respectively. The survey spectra of Cu:Ni:PCF (Figure 3c) showed the presence of both Cu 2p and Ni 2p peaks along with enhanced O 1s intensity, confirming the successful co-deposition of copper and nickel oxides on the PCF surface High-resolution Cu2p spectrum of the Cu_2O/CuO PCF revealed a dominant Cu $2p_3/_2$ peak centered at ~932.4 eV (Figure 3d), characteristic of Cu(I) species[41], along with higher binding energy, weak satellite peaks at 941.2 eV and 943.7 eV. These satellite peaks are a fingerprint of Cu(II), confirming the partial oxidation of Cu_2O to CuO and the coexistence of mixed Cu(I)/Cu(II) oxidation states at the surface.[42] The corresponding peak fitting parameters, including binding energies and FWHM values, are summarized in Table S1 (Supporting Information).Ni 2p spectrum of Ni:PCF showed distinct Ni $2p_3/_2$ and Ni $2p_1/_2$ peaks centered at 854.6 and 872.2 eV, respectively, accompanied by satellite features at higher energy regions. (Figure 3e), which are characteristic of Ni(II) in cubic NiO.[43,44] The Cu:Ni:PCF composite showed Cu $2p_3/_2$ and Cu $2p_1/_2$ peaks shifted to higher binding energies (~933.6 eV and ~953.4 eV), accompanied by distinct satellite features in the 940–945 eV region (Figure 3f). Compared

View Article Online
DOI: 10.1039/D6NH00181E

to Cu_2O/CuO:PCF, this positive shift suggests electronic interaction between Cu and Ni oxide species, resulting in interfacial charge redistribution and modification of the local electron density around Cu centers. Such behavior is commonly observed in mixed-metal oxide systems where electronic coupling occurs at the Cu–Ni oxide interface. The co-existence of Cu(I) and Cu(II) species inferred from XPS is consistent with the XRD results and indicates the presence of mixed Cu_2O/CuO phases integrated within the carbon fiber matrix. The resulting heterogeneous metal oxide environment may contribute to enhanced surface polarity and stronger interactions with dye molecules. Here, nickel predominantly exists in the Ni(II) oxidation state and remains chemically stable after integration with copper oxides and carbon fibers (Figure 3g).

Effect of pH and Initial Dye Concentration on Adsorption Performance

Solution pH plays a critical role in governing adsorption behavior, as it regulates both the ionization characteristics of dye molecules and the surface charge properties of the adsorbent. To systematically evaluate this effect, the adsorption capacities of PCF, Cu:PCF, Ni:PCF, and Cu:Ni:PCF were assessed over a pH range of 2–10 for MO and MB (Figure 4). To ensure reproducibility and minimize experimental variance, pH-dependent adsorption studies were systematically performed in independent triplicates, with the corresponding statistical trends and error bars presented in the Supporting Information (Figure S4). For MO, all adsorbents showed a clear decrease in adsorption capacity with increasing pH, with maximum uptake occurring under strongly acidic conditions at pH 2 (Figure 4a). Among the adsorbents, Cu:Ni:PCF exhibited the highest adsorption capacity (~362.0 ± 8.5 mg g^{-1}), followed by Cu:PCF, PCF, and Ni:PCF at lower pH. This behaviour is due to increased electrostatic attraction between anionic sulfonate groups of MO and protonated surface sites (e.g., $–OH_2^+$) in acidic media. Elevated pH conditions promote the deprotonation of surface functional groups and lead to the development of net negative charges on surfaces, which results in electrostatic repulsion with the anionic dye, thus reducing adsorption capacity.[45] Additionally, the increasing amount of hydroxide ions at higher pH competes with dye molecules for available adsorption sites, further hindering MO uptake. The better performance at lower pH, particularly Cu:Ni:PCF, may be attributed to localized positive charges at Cu centers, which enhance Lewis acid-base interactions with dye molecules.

MB adsorption improved with higher pH, which is consistent with its cationic nature (Figure 4b). With increasing pH, deprotonation of surface groups generated a negatively charged

View Article Online
DOI: 10.1039/D6NH00181E

surface, which enhanced electrostatic attraction and improved MB uptake. Among the adsorbents, Ni:PCF and Cu:Ni:PCF displayed the highest adsorption capacities under basic conditions, likely due to Ni sites capable of redox activity, leading to a higher surface electron concentration. The ζ-potential of Cu:Ni:PCF varied from +31 mV at pH 2 to −32 mV at pH 10, with a point of zero charge (pH_{PZC}) near 5.5 (Figure S5). This surface charge reversal correlated the adsorption trends observed for anionic MO and cationic MB, confirming that electrostatic interactions primarily govern dye binding while π–π stacking and Lewis acid-base coordination maintain adsorption across a broad pH range. The combination of Cu and Ni oxides appeared to modulate surface charge distribution, enhance functional group diversity, and increase the density of accessible adsorption sites.

To investigate the adsorption behaviour as a function of initial dye concentration, isotherm studies were conducted using MO and MB at concentrations ranging from 25 to 300 mg L^{-1}. The equilibrium adsorption capacities (Q_e) of PCF, Cu:PCF, Ni:PCF, and Cu:Ni:PCF for MO and MB are presented in Figure 4(c-d). For MO, Q_e increased with initial dye concentration and approached saturation at higher levels, consistent with Langmuir-type monolayer adsorption (Figure 4c). Among all tested materials, Cu:Ni:PCF exhibited the highest capacity (~190 mg g^{-1}). The superior performance of Cu:Ni:PCF is attributed to the greater density of active sites, enhanced surface polarity, and dual metal synergy that introduces defect sites and strengthens electrostatic and Lewis acid-base interactions with the anionic dyes. The observed saturation behaviour at higher concentrations is indicative of monolayer adsorption, consistent with Langmuir isotherm characteristics, implying that the number of active sites is finite and uniformly distributed. For MB, a similar concentration-dependent increase in Q_e was observed, plateauing at higher concentrations due to saturation of the surface sites (Figure 4d). Ni:PCF and Cu:Ni:PCF displayed the highest capacities (~95 and ~105 mg g^{-1}, respectively), reflecting favorable electrostatic attraction, π–π stacking, and coordination between Ni sites and the cationic dye. Co-doping with Cu and Ni effectively tailored surface charge distribution and functional group heterogeneity, enabling strong interactions with both anionic and cationic dyes. This phenomenon suggests that the adsorption mechanism is influenced by both physical (diffusion, π–π stacking) and chemical interactions (electrostatic, Lewis acid–base, metal–dye complexation), which are synergistically optimized in the bimetallic Cu:Ni:PCF. Metal doping, particularly co-doping, can significantly enhance the adsorption performance of porous carbon frameworks for both anionic and cationic dye pollutants.[46]

View Article Online
DOI: 10.1039/D6NH00181E

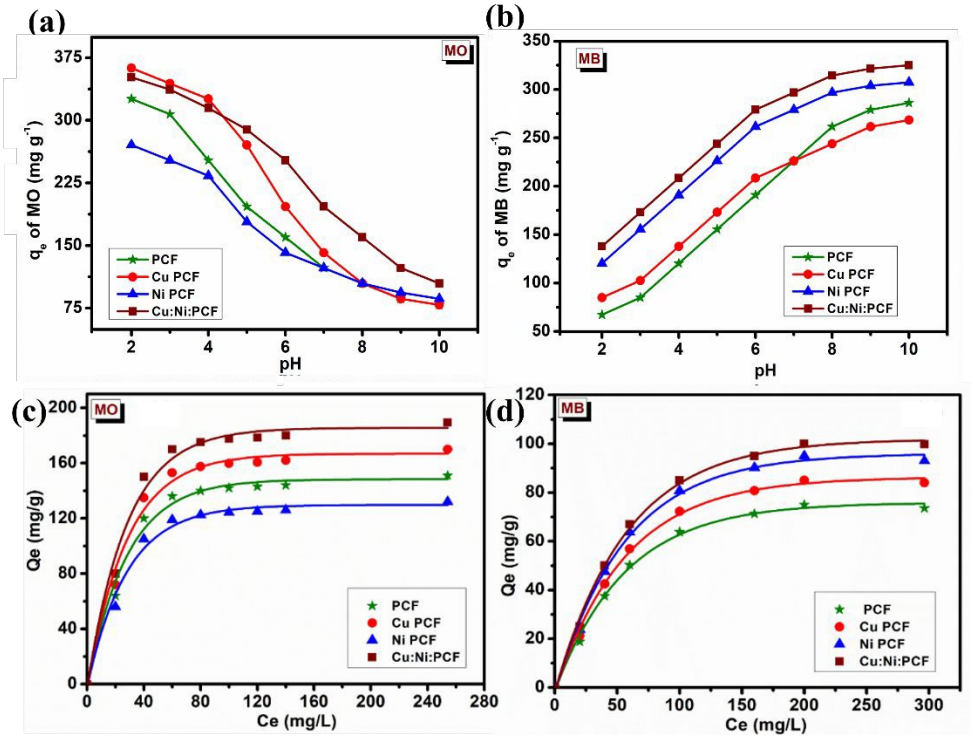

Figure 4 (a-b) Effect of the initial pH value on the adsorption performance of MO and MB, (c-d) Effect of initial dye concentration of MO and MB by PCF, Cu_2O/CuO-PCF, NiO-PCF and Cu:Ni:PCF.

To understand the adsorption kinetics and real-time dye removal efficiency of the Cu:Ni:PCF composite, time-dependent UV–Vis absorbance spectra were recorded for MO and MB at regular intervals. These spectra represent the progressive decrease in characteristic absorbance intensity of the respective dyes, corresponding to their degradation from aqueous solution over time. For MO (Figure 5a), the maximum absorbance peak centered around ~465 nm gradually diminished with time, indicating efficient adsorption of the dye molecules onto the Cu:Ni:PCF surface. A significant reduction in peak intensity was observed within the first 10 min, suggesting rapid initial adsorption, likely driven by strong electrostatic attraction between the negatively charged sulfonate groups of MO and the positively charged functional sites on the adsorbent under acidic conditions. After ~16 min, the absorbance plateaued near baseline, indicating almost complete removal of MO from the solution. A similar trend was observed for MB (Figure 5b), with the primary absorption band located around ~665 nm. Although the adsorption of MB was a little slower compared to MO, substantial decolorization was achieved within 18 min. Enhanced MB adsorption results from similar electrostatic attraction and π–π

View Article Online
DOI: 10.1039/D6NH00181E

interactions between the cationic dye and the negatively charged, graphitic Cu:Ni:PCF surface under basic conditions. These results confirm the high adsorption efficiency and fast kinetics of Cu:Ni:PCF. The rapid dye removal highlights Cu:Ni:PCF suitability for fast and efficient wastewater treatment applications.

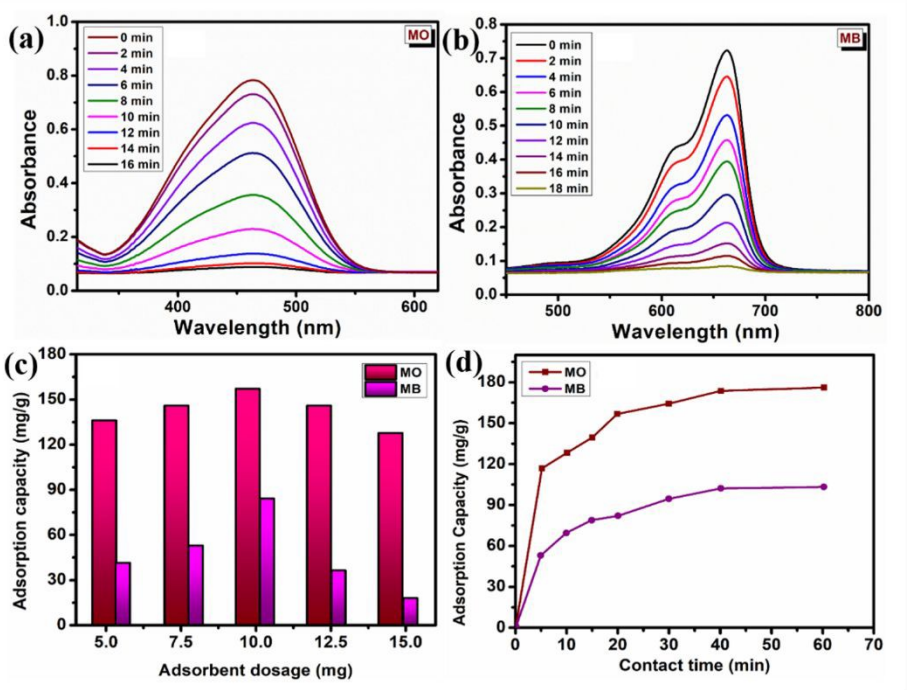

Figure 5 UV-Vis spectra of aqueous dye solutions (a) MO and (b) MB at various adsorption times. (c) Effect of dosage on the adsorption of MO and MB by Cu:Ni:PCF. (d) Effect of contact time on adsorption of MO and MB by Cu:Ni:PCF.

Effect of Adsorbent Dosage and Time

To understand the adsorption behaviour of MO and MB dyes, the influence of adsorbent dosage and contact time was systematically investigated. Adsorption experiments were conducted by varying the adsorbent mass (5-15 mg) while keeping the dye concentration (200 mg L^{-1}) and pH constant. MO showed higher adsorption capacity than MB since protonated –OH sites favoured interaction with MO sulfonate and azo groups, while MB experienced partial electrostatic repulsion. Additionally, MO's planar structure enabled faster diffusion and stronger conjugation with the graphitic matrix, whereas MB's bulkier geometry and cationic nature limited adsorption efficiency. As shown in Figure 5c, a significant increase in adsorption capacity (Q_e) was observed as the dosage increased from 5 to 10 mg for all materials due to the greater availability of active adsorption sites and larger surface area. Among all the adsorbents, Cu:Ni:PCF exhibited the highest Q_e values, reflecting the synergistic effects of dual metal

View Article Online
DOI: 10.1039/D6NH00181E

doping in improving surface charge distribution, electronic conductivity, and defect site density. However, further increasing the dosage to 15 mg led to a decline in Q_e. This decrease was primarily due to particle aggregation at higher loadings, which reduced the effective surface area along with saturation of available adsorption sites. Thus, 10 mg was identified as the optimal dosage, balancing surface accessibility and adsorption efficiency. The time-dependent adsorption was evaluated using 10 mg of adsorbent in 50 mL of 200 mg L^{-1} dye solution at neutral pH (Figure 5d). A rapid uptake occurred within the first 15 min due to the high concentration gradient and abundant active sites, followed by a slower approach to equilibrium at ~60 min, indicating surface site saturation as the rate-limiting step.[47] Cu:Ni:PCF showed the highest equilibrium capacity for MO (176.2 mg g^{-1}) than MB (102.8 mg g^{-1}), attributed to differences in molecular size, charge distribution, and interaction strength. The superior kinetics and capacity of Cu:Ni:PCF are resulted from its mesoporous structure, high surface area, and metal-induced active sites, confirming its efficiency as a fast, robust, and multifunctional adsorbent for dye removal.

Adsorption isotherm analysis

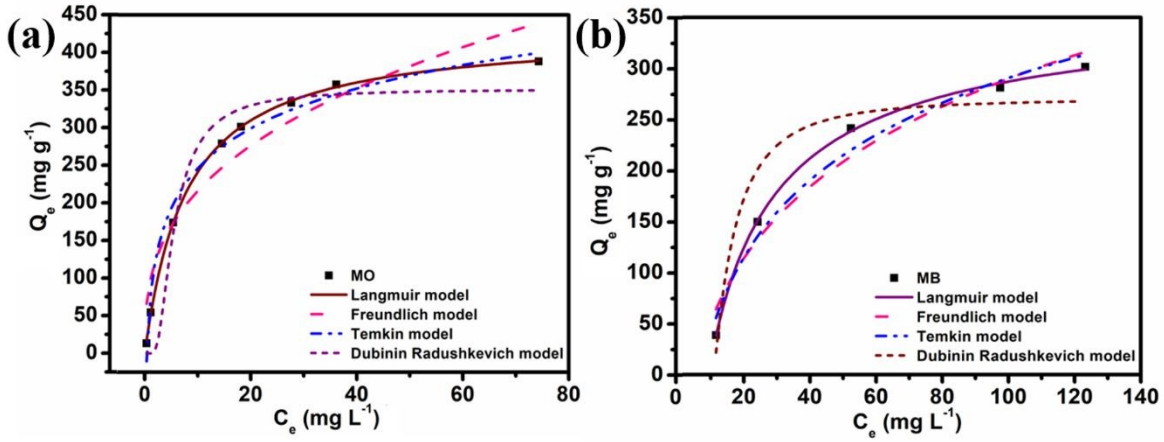

Figure 6 Equilibrium adsorption isotherms of (a) MO and (b) MB on Cu:Ni:PCF.

The equilibrium adsorption isotherms of Cu:Ni:PCF at 298 K were obtained over a wide concentration range (25–300 mg L^{-1}) of MO and MB (Figure 6). The isotherms displayed a rapid increase in adsorption capacity at low equilibrium concentrations, reflecting strong dye surface interactions and the preferential occupation of high-energy active sites. At higher solute concentrations, the uptake levelled off, reflecting the saturation of adsorption sites and the establishment of equilibrium. The experimental data were fitted using Langmuir, Freundlich, Temkin, and Dubinin–Radushkevich models to identify the dominant adsorption

View Article Online
DOI: 10.1039/D6NH00181E

mechanism.[48-50] Among these, the Langmuir model shows the highest correlation coefficients for both dyes (R^2 = 0.994 for MO and 0.991 for MB; Table S2), demonstrating superior agreement with the experimental results. This strong correlation suggests that adsorption proceeds mainly through monolayer formation on a surface with energetically uniform active sites. The dominance of Langmuir behaviour can be attributed to the homogeneous distribution of Cu and Ni oxide species within the porous carbon fiber matrix, which provides uniformly accessible adsorption sites and minimizes interaction effects.

Adsorption kinetic analysis

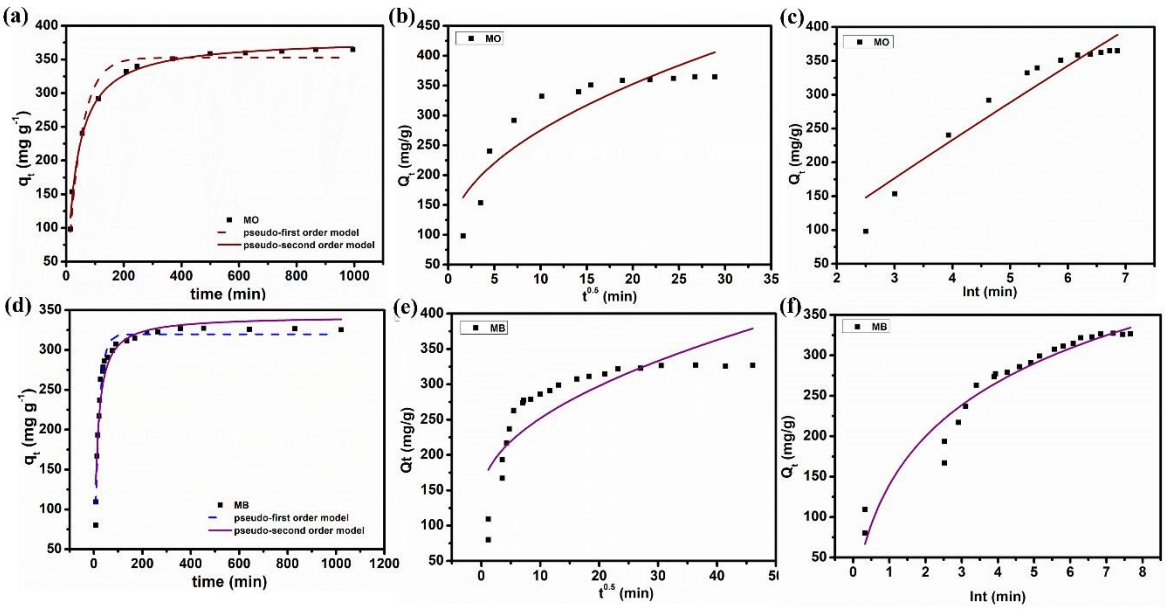

Figure 7 Kinetic models of MO and MB adsorption on Cu:Ni:PCF: (a, d) pseudo-first-order and pseudo-second-order fits, (b, e) Weber–Morris intra-particle diffusion plots model, and (c, f) Elovich model, where panels (a–c) and (d–f) correspond to MO and MB, respectively.

Among the evaluated kinetic models, the pseudo-second-order model provided the best fit for both MO and MB, as indicated by the highest correlation coefficients (R^2 = 0.994 for MO and 0.993 for MB, Table S3). Moreover, the calculated equilibrium adsorption capacities ($q_{e,cal}$ = 365 mg g^{-1} for MO and 325 mg g^{-1} for MB) closely agreed with the experimental values, confirming the robustness of this model in describing the adsorption process. In contrast, the pseudo-first order, Elovich and Weber–Morris models showed poorer fits and were therefore not suitable for accurately representing the adsorption kinetics in this system. To further

View Article Online
DOI: 10.1039/D5NH00181E

contextualize the adsorption performance of the Cu:Ni:PCF, a comparison with previously reported adsorbents for dye removal is summarized in Table 1.

Table 1. Comparison of adsorption performance of Cu:Ni:PCF with carbon-based adsorbents for MO and MB

Adsorbent	Dye	q_{max} (mg g^{-1})	Contact Time (min)	Ref
Activated carbon	MO	194	~120	[51]
Chitosan/graphene oxide composite	MO	210	~90	[52]
Fe3O4/biochar composite	MB	238	~50	[53]
N-doped porous carbon fiber	MB	276	~40	[54]
ZnO–C composite	MO	365	~60	[55]
MgO-biochar nanocomposite	MB	312	~40	[56]
Cu:Ni:PCF	MO	362	~15	**This work**
Cu:Ni:PCF	MB	323	~15	**This work**

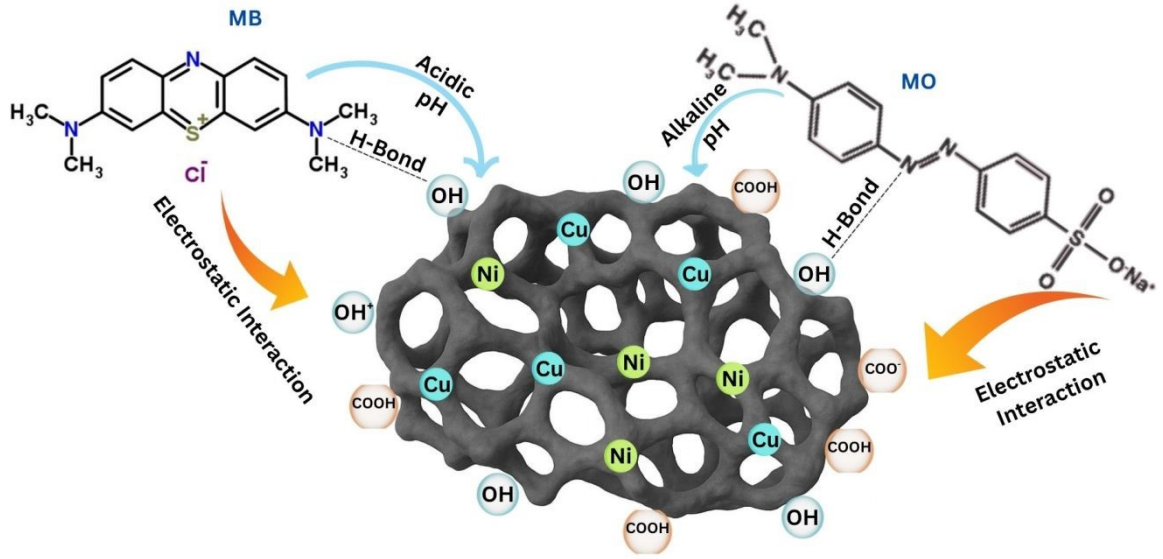

Figure 8 Schematic representation of the adsorption mechanism of MB and MO on Cu:Ni:PCF.

The superior adsorption performances of Cu:Ni:PCF toward both anionic and cationic dyes are because of a combination of physicochemical interactions and structural features imparted by dual-metal doping (Figure 8). Electrostatic interaction is a primary governing mechanism, modulated by solution pH. Under acidic conditions, surface functional groups such as –OH undergo protonation, rendering the adsorbent surface positively charged and thus preferably adsorb anionic dyes like methyl orange (MO) through electrostatic attraction. Conversely, at

View Article Online
DOI: 10.1039/D6NH00181E

alkaline pH, deprotonation leads to a negatively charged surface that enhances the adsorption of cationic dyes (e.g., methylene blue or MB). In addition to charge-based interactions, π–π stacking occurs between the aromatic rings of dye molecules and the graphitized carbon domains within the adsorbent, contributing significantly to dye immobilization.[57] The incorporation of Cu and Ni further introduces Lewis acidic sites capable of forming coordination bonds with electron-rich functional groups present in dye molecules, strengthening the adsorption affinity.[58] Notably, redox-active Ni centers may facilitate partial electron transfer interactions, enhancing MB adsorption through redox stabilization.[59] Moreover, the residual oxygen-containing functionalities (e.g., –OH and –COOH) on the PCF participate in hydrogen bonding with polar groups in dye molecules, further stabilizing the adsorbed species.[60] The synergistic effect of dual metal doping not only enhances the density and diversity of active sites but also introduces surface defects and charge heterogeneity, resulting in improved adsorption across a broad pH range.[61] Collectively, these interactions lead to multifunctional adsorption behavior of Cu:Ni:PCF, making it a robust and versatile adsorbent for wastewater treatment applications.

Adsorption thermodynamics

To gain further insight into the nature of the dye adsorption process, thermodynamic feasibility and nature of MO and MB adsorption onto Cu:Ni:PCF were evaluated using Van't Hoff analysis by correlating ln K_d with temperature (298 K, 313 K, 328 K). The derived thermodynamic values are compiled in Table 2. Using the Van't Hoff plot (ln K vs. 1/T), ΔH° was obtained from the slope, while ΔS° was derived from the intercept. For both dyes, the Gibbs free energy change (ΔG°) values were negative, confirming that adsorption proceeds spontaneously.[62] Moreover, with rising temperature, the ΔG° values dropped further, which reflects that elevated temperatures favor dye uptake. The positive enthalpy change (ΔH°) values of 24.8 kJ mol^{-1} for MO and 31.6 kJ mol^{-1} for MB indicate that the adsorption process is endothermic in nature.[63] The higher ΔH° observed for MB suggests stronger temperature-dependent interactions, consistent with its bulkier molecular structure and enhanced sensitivity to surface rearrangements. The positive entropy change (ΔS°) values further indicate an increase in randomness at the solid-liquid interface during adsorption, which may arise from the displacement of solvated water molecules and structural reorganization of dye molecules upon binding to heterogeneous adsorption sites.[64] Notably, the Van't Hoff graphs exhibited localized downward deviations at 313 K, more pronounced for MB, reflecting non-ideal thermodynamic behavior. Such non-linearity may arise from several factors, including minor

View Article Online
DOI: 10.1039/D6NH00181E

experimental uncertainty, partial desorption–readsorption effects, transient site competition, or subtle changes in adsorbate–surface interactions.[65] Unlike many reports that assume ideal linear Van't Hoff behavior, the present system exhibits localized non-linearity at intermediate temperature (313 K), particularly for MB.[66] Such behavior has been increasingly recognized in heterogeneous and multifunctional adsorbents, where temperature-dependent surface restructuring, hydration effects, and competitive site occupation influence adsorption energetics. Importantly, the overall thermodynamic trends remain unchanged, and the localized deviation does not significantly affect the calculated thermodynamic parameters. This distinction underscores the advantage of hetero-porous frameworks in real wastewater treatment scenarios.

Table 2. Thermodynamic parameters for MO and MB adsorption on Cu:Ni:PCF

Adsorbate	ΔH (KJ mol^{-1})	ΔS (J mol^{-1} K^{-1})	ΔG (KJ mol^{-1})		
			298 K	313 K	328 K
MO	24.8	105	-6.57	-5.59	-4.78
MB	31.6	121	-5.08	-3.77	-3.69

Reusability

After maximum desorption at their respective pH values, the adsorbent was submerged for 24 h for desorption, followed by re-adsorption up to 5 cycles (Figure 9). Good regeneration capability in an adsorbent not only reduces pretreatment expenses but also improves its reusability, making it highly valuable for real-world dye removal from wastewater. As observed in the bar diagram, the efficiency of the adsorbent remained intact up to 5 cycles for both dyes. The adsorption efficiency of both dyes in the fifth cycle remained above 90%. The XPS spectra recorded after the fifth adsorption cycle showed slight shifts in the Cu 2p and Ni 2p binding energies (Figure S6), indicating the involvement of Cu and Ni oxide active sites in dye adsorbent interactions during adsorption. The Cu 2p and Ni 2p spectra retained their characteristic features, confirming the preservation of the Cu/Ni oxide phases. Minor shifts in the binding energies of the Cu 2p and Ni 2p peaks were observed, indicating slight changes in the local electronic environment of the metal oxide active sites after repeated adsorption. These shifts suggest the participation of Cu and Ni oxide domains in dye–surface interactions during adsorption. Nevertheless, the absence of significant spectral changes and the retention of the characteristic satellite features demonstrate the good chemical stability of the Cu:Ni framework during repeated adsorption–desorption cycles.

View Article Online
DOI: 10.1039/D6NH00181E

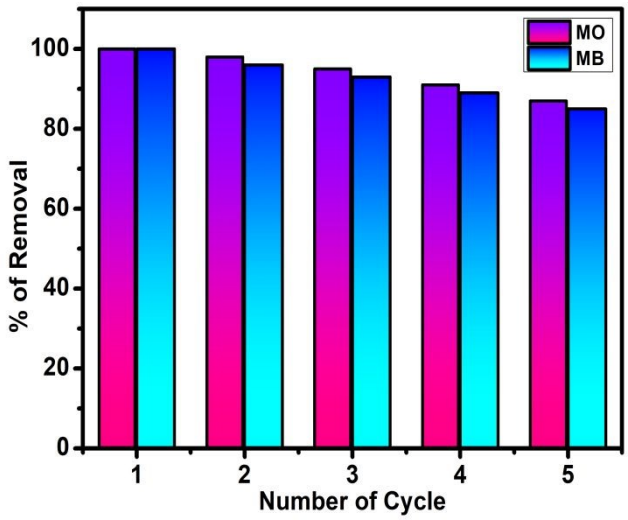

Figure 9. Recyclability for MO and MB dye adsorption by Cu:Ni:PCF.

Mixed Dye Adsorption

Industrial wastewater often contains mixtures of dyes, necessitating the development of adsorbents capable of simultaneously and selectively removing multiple dye species, either via physical sorption or covalent bonding[67]. For evaluating the real-world applicability of the synthesized Cu:Ni:PCF, mixed dye adsorption studies were conducted under near-neutral conditions (pH ≈ 7). Equal volumes of MO & MB dye solutions were mixed and treated with 10 mg of Cu:Ni:PCF. A pronounced reduction in the characteristic absorption band of MB was observed, while the MO absorption peak remained relatively prominent after adsorption (Figure 10), indicating preferential adsorption of the cationic MB dye in the mixed-dye system. This behavior is attributed mainly to pH-dependent electrostatic interactions between the dye molecules and the Cu:Ni:PCF surface under near-neutral conditions. These findings demonstrate preferential adsorption behavior toward MB in the presence of MO, highlighting the influence of competitive adsorption effects in mixed dye systems[68].

View Article Online
DOI: 10.1039/D6NH00181E

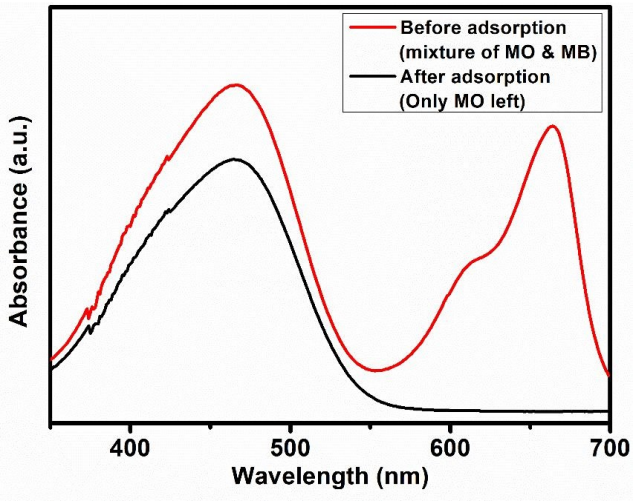

Figure 10 UV–vis spectra of selective dye adsorption by Cu:Ni:PCF.

Conclusion

This work demonstrates a rational design of bimetallic copper/nickel oxide doped porous carbon nanofibers (Cu:Ni:PCF) as a highly efficient adsorbent for remedying dye-contaminated wastewater. The integration of RAFT polymerization, electrospinning, and controlled pyrolysis enabled the fabrication of a hierarchically porous carbon network uniformly decorated with copper and nickel oxide nanoparticles, generating chemically diverse and heterogeneous adsorption sites. Such structural synergy translated into outstanding bifunctional adsorption performance toward both MO and MB dyes, with maximum adsorption capacities of 362.0 ± 8.5 mg g^{-1} for MO and 323.0 ± 7.2 mg g^{-1} for MB. Mechanistic evaluation revealed that adsorption was governed by a cooperative interplay of electrostatic attraction, π–π interactions, Lewis acid–base coordination, and hydrogen bonding, further modulated by redox-active metal centres. Kinetic and isotherm analyses confirmed pseudo-second-order behavior and Langmuir monolayer adsorption, while thermodynamic parameters established the spontaneous and endothermic nature of dye uptake. The material exhibited excellent recyclability with preserved chemical structure, and preferential adsorption of MB in mixed-dye systems highlighted its competitive adsorption behavior. Importantly, the present study extends beyond the use of block-copolymer-derived porous carbon fibers as structural templates by integrating synergistic Cu_2O/CuO and NiO domains to create multifunctional adsorption interfaces capable of interacting with both anionic and cationic dyes. Overall, this study advances bimetallic carbon nanofiber engineering as a scalable and robust platform for wastewater treatment applications.

View Article Online
DOI: 10.1039/D6NH00181E

Author Contribution

A.P. Parekh: Conceptualization, experiments, characterization, data analysis, scientific discussion, original draft writing, review, and editing. **S. Jain:** Conceptualization, scientific discussion, and editing. **V. Sharma:** reviewing manuscript. **Y. Zhang:** Characterization and reviewing. **G. Liu:** Conceptualization, experimental design, scientific discussion, supervision, review, and editing.

Data availability

Characterization of synthesized block co-polymer, pore size distribution, XPS survey spectra, ζ-potential, XPS spectra, Fitting Parameters of Langmuir, Freundlich Models, Temkin Model and Dubinin-Radushkevich for MO and MB adsorption by Cu:Ni:PCF, and Fitting Parameters of Pseudo first order, Pseudo Second order, Elovich and Weber-Morris for MO and MB adsorption by Cu:Ni:PCF.

Conflicts of interest

There are no conflicts to declare.

Acknowledgments

This work is partially based on the project supported by NSF Award No. DMR-2411680. We acknowledge the use of the Nanoscale Characterization and Fabrication Laboratory (NCFL) and chemistry facilities at Virginia Tech, USA.

View Article Online
DOI: 10.1039/D6NH00181E

References:

1. M. H. Khorasanizadeh, M. Hajizadeh-Oghaz, A. Khoobi, S. H. Ganduh, M. A. Mahdi, W. K. Abdulsahib, L. S. Jasim, M. Salavati-Niasari, *Int. J. Hydrogen Energy,* 2022, **47** (46), 20112−20128.
2. A. Zafar, S. Ullah, M. T. Majeed, R. Yasmeen, *OPEC Energy Rev.* 2020, **44**, 227−248.
3. R. Rahimi, H. Kerdari, M. Rabbani, M. Shafiee, *Desalination* 2011, **280**, 412−418.
4. S. P. Buthelezi, A. O. Olaniran, B. Pillay, *Molecules*, 2012, **17**, 14260−14274.
5. W. M. Warren-Vega, A. Campos-Rodríguez, A. I. Zárate-Guzmán, L. A. Romero-Cano, *Int. J. Environ. Res. Public Health* 2023, **20**, No. 4499.
6. R. Al-Tohamy, S. S. Ali, F. Li, K. M. Okasha, Y. A. G. Mahmoud, T. Elsamahy, H. Jiao, Y. Fu, J. Sun, *Ecotoxicol. Environ. Saf.* 2022, **231**, No. 113160.
7. P. O. Oladoye, T. O. Ajiboye,E. O. Omotola, O. J. Oyewola, *Results Eng.* 2022, **16**, No. 100678.
8. S. K. Dutta, M. K. Amin, J. Ahmed, Md. Elias, Md. Mahiuddin, *S. Afr. J. Chem. Eng.* 2022, **40**, 195−208.
9. B. Rani, R. Maheshwari, R. K. Yadav, D. Pareek, A. Sharma, *Res. J. Chem. Environ. Sci.* 2013, **1** (1), 50−54.
10. P. P. Mon, P. P. Cho, H. S. Rangappa, S. Dobhal, P. Ghosal, G. Madras, S. Ch, *J. Phys. Chem. B* 2024, **128**, 8223−8237.
11. S. Soyer-Uzun, P. Yu, F. K. Öner, S. Sen, *J. Phys. Chem. B* 2024, **128**, 12638−12650.
12. R. Kumar, M. Ehsan,M. A. Barakat, *J. Ind. Eng. Chem.* 2014, **20**, 4202−4206.
13. X. Tao, C. Yang, Z. Wei, L. Huang, J. Chen, W. Cong, R. Xie, D. Xu, *Mater. Res. Bull.* 2019, **120**, No. 110581.
14. A. B. Isaev, N. S. Shabanov, A. G. Magomedova, P. V. Nidheesh, M. A. Oturan, *Environ. Chem. Lett.* 2023, **21**, 2863−2911.
15. K. Singh, P. Kumar, R. Srivastava, *Pollut. Res.* 2017, **36**, 790−797.
16. K. M. Katubi, N. Shaheen, S. Zulfiqar, N. Irshad, Z. A. Alrowaili, I. S. Al-Buriahi, I. Shakir, M. F. Warsi, E. W. Cochran, *Ind. Eng. Chem. Res.* 2024, **63** (27), 11922−11938.
17. L. Zeng, F. Zhe, Y. Wang, Q. Zhang, X. Zhao, X. Hu, Y. Wu, Y. He, *J. Colloid Interface Sci.* 2019, **539**, 563−574.
18. B. Li, F. Mumtaz, X. Li, M. R. Al Shehhi, K. Wang, *Chem. Eng. J.* 2023, **470**, No. 144369.
19. M. El-Shahat, A. E. Abdelhamid, R. M. Abdelhameed, *Carbohydr. Polym.* 2020, **231**, No. 115742.
20. W. P. Mounfield III, M. Taborga Claure, P. K. Agrawal, C. W. Jones, K. S. Walton, *J. Ind. Eng. Chem.* 2016, **55**, 6492-6500.
21. Q. Bao, C. M. Li, L. Liao, H. Yang, W. Wang,C. Ke, Q. Song,H. Bao, T. Yu, K. P. Loh, J. Guo, *Nanotechnology* 2009, **20**, 065203–065210.
22. Y. B. Zhang, J. Yin, L. Li, L. X. Zhang, L. J. Bie, *Sens. Actuators B Chem.* 2014, **202**, 500–507.
23. A. P. Parekh, C. Posada, N. Karmakar, S. Jain, G. Liu, *Appl. Electron. Mater.* 2025, **7**, 24, 11027-11037.
24. M. Yu, H. Dong, Y. Zheng, W. Liu, *Chemosphere*, 2021, **280**, 130567-130576.
25. Y. Zhu, S. Murali, M. D. Stoller, K. J. Ganesh, W. Cai, P. J. Ferreira, A. Pirkle, R. M. Wallace, K. A. Cychosz, M. Thommes, D. Su, E. A. Stach, R. S. Ruoff, *Science*, 2011, **332**, 1537–1541.
26. G. Wang, H. Wang, X. Lu, Y. Ling, M. Yu, T. Zhai, Y. Tong, Y. Li, *Adv. Mater.* 2014, **26**, 2676–2682.
27. Z. Zhou, T. Liu, A. U. Khan, G. Liu, *Sci. Adv.* 2019, **5**, eaau6852.

28. A. P. Parekh, A. K. Yadav, B. Whitfield, Y. Zhang, A. Aijaz, G. Liu, *Appl. Eng. Mater.* 2025, **3**, 4167−4177.
29. J. M. Serrano, T. Liu, A. U. Khan, B. Botset, B. J. Stovall, Z. Xu, D. Guo, K. Cao, X. Hao, S. Cheng, G. Liu, *Chem. Mater.* 2019, **31** (21), 8898– 8907.
30. B. J. Ostertag, M. T. Cryan, J. M. Serrano, G. Liu and A. E. Ross, *ACS Appl. Nano Mater.*, 2022, **5**, 2241–2249.
31. M. Zhong, C. Tang, E. K. Kim, M. Kruk, E. B. Celer, M. Jaroniec, K. Matyjaszewski, T. Kowalewski, *Mater. Horizons*, 2014, **1**, 121–124.
32. J. M. Serrano, A. U. Khan, T. Liu, Z. Xu, A. R. Esker, G. Liu, *Adv. Mater. Interfaces*, 2020, **7** (16), 2000507.
33. Y. Guan, H. Y. Yu, S. Y. H. Abdalkarim, C. Wang, F. Tang, J. Marek, W. L. Chen, J. Militky, J. M. Yao, *Int. J. Biol. Macromol.* 2019, **132**, 51−62.
34. H. Al-Zoubi, M. Zubair, M. S. Manzar, A. A. Manda, N. I. Blaisi, A. Qureshi, A. Matani, *Arab. J. Sci. Eng.* 2020, **45**, 7275−7287.
35. A. Paton-Carrero, P. Sanchez, L. Sanchez-Silva, A. Romero, *Mater. Today Commun.* 2022, **30**, No. 103033.
36. K. Dai, N. Zhang, L. Zhang, L. Yin, Y. Zhao, B. Zhang, *Chem. Eng. J.* 2021, **414**, 128804.
37. Y. Qin, J. Zhang, Y. Wang, X. Shu, C. Yu, J. Cui, H. Zheng, Y. Zhang, Y. Wu, *RCS Adv.* 2016, **6**, 47669–47675.
38. L. M. Peddada, P. P. Cho, S. Dulgaj, R. Annapragada, P. R. Kanuparthy, *Results in Optics.* 2023, **13**, 100537.
39. S. Chatterjee, A. Ray, M. Mandal, S. Das, S. K. Bhattacharya, *J. Mater. Eng. Perform.* 2020, **29**, 8036–8048.
40. G. S. Armatas, D. E. Petrakis, P. J. Pomonis, *Microporous Mesoporous Mater.* 2005, **83**, 251−261.
41. S. Poulston, P. M. Parlett, P. Stone, M. Bowker, *Surf. Interface Anal.* 1996, **24**, 811-820.
42. J. Ghijsen, L. H. Tjeng, J. V. Elp, H. Eskes, J. Westerink, G. A. Sawatzky, M. T. Czyzyk, *Phys. Rev. B: Condens. Matter*, 1988, **38**, 11322–11330.
43. C. S. Lei, X. F. Zhu, B. C. Zhu, J. G. Yu, W. K. Ho, *J. Colloid Interface Sci.* 2016, **466**, 238–246.
44. F. Yang, J. Yao, F. Liu, H. He, M. Zhou, P. Xiao, Y. Zhang, *J. Mater. Chem. A.* 2013, **1**, 594-601.
45. Y. Bai, X. Gan, Z. Jing, P. Fan, *Langmuir* 2025, **41**, 34, 22723-22737.
46. H. Wang, Z. Li, S. Yahyaoui, H. Hanafy, M. K.Seliem, A. B. Petriciolet, G. L. Dotto, L. Sellaoui, Q. Li, *Chem. Eng. J.* 2021, **417,** 128116.
47. I. Tan, A. Ahmad, B. Hameed, 2008, **154**, 337–346.
48. V. Jeyavani, S. P. Mukherjee, *Inorg. Chem.* 2022, **61**, 18119−18134.
49. Z. Liu, X. Huang, Y. Miao, B. Gao, Y. Shi, J. Zhao, S. H. Tan, *Ind. Crops Prod.* 2022, **187**, No. 115510.
50. M. A. Islam, M. J. Ahmed, W. A. Khanday, M. Asif, B. H. Hameed, *Ecotoxicol. Environ. Saf.* 2017, **138**, 279−285.
51. S. Wang and H. Li, *J. Hazard. Mater.*, 2007, **147**, 77–84.
52. I. A. W. Tan, A. L. Ahmad and B. H. Hameed, *J. Hazard. Mater.*, 2008, **154**, 337–346.
53. F. Reguyal and A. K. Sarmah, *J. Hazard. Mater.*, 2018, **321**, 868–878.
54. M. Zhang, B. Gao, Y. Yao, Y. Xue and M. Inyang, *Chem. Eng. J.*, 2012, **210**, 26–32.–
55. R. Ahmad, R. Kumar, *J. Environ. Chem. Eng.* 2021, **9**, 105123.
56. M. Zhang, B. Gao, Y. Yao, Y. Xue and M. Inyang, *Chem. Eng. J.*, 2012, **210**, 26–32.

57. H. Zhao, X. Liu, Z. Cao, Y. Zhan, X. Shi, Y. Yang, J. Zhou, J. Xu, *J. Hazard. Mater.* 2016, **310**, 235–245.
58. J. Shu,S. Cheng, H. Xia, L. Zhang, J. Peng, C. Li, S. Zhang, *RSC Adv*. 2017, **7**, 14395–14405.
59. Y. Zhang, Y. Li, M. Wang, B. Chen, Y. Sun, K. Chen, Q. Du, X. Pi, Y. Wang, *Nanomaterials*, 2022, **12**, 2533.
60. H. Li, L. Liu, J. Cui, F. Wang, F. Zhang, *RSC Adv*. 2020, **10**, 14262–14270.
61. Y. S. Reddy, N. K. Rotte, S. Hussain, V. V. S. S. Srikanth, M. R. Chandra, *J. Hazard. Mater. Adv.* 2023, **9**, 100214.
62. H. Guedidi, L. Reinert, J. M. Lévêque, Y. Soneda, N. Bellakhal, L. Duclaux, *Carbon*, 2013, **54**, 432–443.
63. A. Samage, M. Halakarni, D. Ghosh, S. K. Nataraj, *Chem. Eng. J.* 2022, **435**, 134952.
64. J. R. Kim, S. G. Huling, E. Kan, *Chem. Eng. J.* 2015, **262**, 1260–1267.
65. Y. Liu, Y. J. Liu, *Sep. Purif. Technol.* 2008, **61**, 229–242.
66. H. N. Tran, S. J. You, A. Hosseini-Bandegharaei, H. P. Chao, *Water Res*. 2017, **120**, 88–116.
67. S. N. Dada, G. K. Babanyinah, M. T. Tetteh, V. E. Palau, Z. F. Walls, K. Krishnan, Z. Croft, A. U. Khan, G. Liu, T. E. Wiese, E. Glotser, H. Mei, ACS Omega 2022, **7**, 27, 23322–23331.
68. Y. Zhan, L. Yang, J. Lan, J. Shang, S. Chen, X. Guan, W. Li, S. Lin, *Cellulose,* 2021, **28**, 453−470.

View Article Online
DOI: 10.1039/D6NH00181E

Data Availability Statement

All data supporting the findings of this study are available within the article and its Supplementary Information (SI). The supplementary data include detailed characterization of synthesized block co-polymer, pore size distribution, XPS survey spectra, ζ-potential, XPS spectra, Fitting Parameters of Langmuir, Freundlich Models, Temkin Model and Dubinin-Radushkevich for MO and MB adsorption by Cu:Ni:PCF, and Fitting Parameters of Pseudo first order, Pseudo Second order, Elovich and Weber-Morris for MO and MB adsorption by Cu:Ni:PCF.